PHYSICAL REVIEW FLUIDS **3**, 074101 (2018)

Static and dynamic fluid-driven fracturing of adhered elastica

Thomasina V. Ball*
BP Institute, Department of Earth Sciences, University of Cambridge, Bullard Laboratories, Madingley Road, Cambridge, CB3 0EZ, United Kingdom

Jerome A. Neufeld
BP Institute, Department of Earth Sciences, Department of Applied Mathematics and Theoretical Physics, University of Cambridge, Bullard Laboratories, Madingley Road, Cambridge, CB3 0EZ, United Kingdom

(Received 1 May 2017; published 26 July 2018)

The transient spreading of a viscous fluid beneath an elastic sheet adhered to the substrate is controlled by the dynamics at the tip where the divergence of viscous stresses necessitates the formation of a vapor tip separating the fluid front and fracture front. The model for elastic-plated currents is extended for an axisymmetric geometry with analysis showing that adhesion gives rise to the possibility of static, elastic droplets and to two dynamical regimes of spreading; viscosity dominant spreading controlled by flow of viscous fluid into the vapor tip, and adhesion dominant spreading. Constant flux experiments using clear, PDMS elastic sheets enable new, direct measurements of the vapor tip and confirm the existence of spreading regimes controlled by viscosity and adhesion. The theory and experiments thereby provide an important test coupling the dynamics of flow with elastic deformation and have implications in fluid-driven fracturing of elastic media more generally.

DOI: 10.1103/PhysRevFluids.3.074101

I. INTRODUCTION

The geometry and propagation of fluid-driven fractures is determined by a competition between the flow of viscous fluid, the elastic deformation of the solid, and the energy required to create new surfaces through fracturing. These processes feature industrially in the hydraulic fracturing of shale [1] but are also commonplace in nature, from magmatic intrusions in the Earth's crust [2,3] to the propagation of cracks at the base of glaciers [4]. The relationship between elastic deformation and adhesion energy has been successfully considered for the development of stretchable electronics made from buckled nanoribbons [5,6]. Similarly, the coupling of viscous spreading and elastic deformation has been analyzed when looking at the dynamics of blisters spreading over a prewetted film [7] with applications to the flow of biofluids through deformable vessels [8] and the suppression of viscous fingering in an elastic-walled Hele-Shaw cell [9]. However, the physical processes underlying the dynamics of the fluid-driven fracturing of thin adhered elastica remain unexplored and unobserved.

The transient spreading of a viscous fluid beneath an adhered elastic sheet is controlled by the dynamics at the tip. The centrality of the physics at the contact line is directly analogous to the capillary-driven spreading of a droplet, where elasticity plays the role of surface tension. Near the front, a large negative pressure gradient is needed to drive the viscous fluid into the narrowing gap of the fracture where the rate of viscous dissipation diverges. This is the elastic equivalent of Huh and Scriven's paradox [10] and theoretically leads to the immobility of the contact line. In the context of a spreading droplet, microscopic mechanisms such as a precursor film [11] and relaxation of the

*tvb21@cam.ac.uk

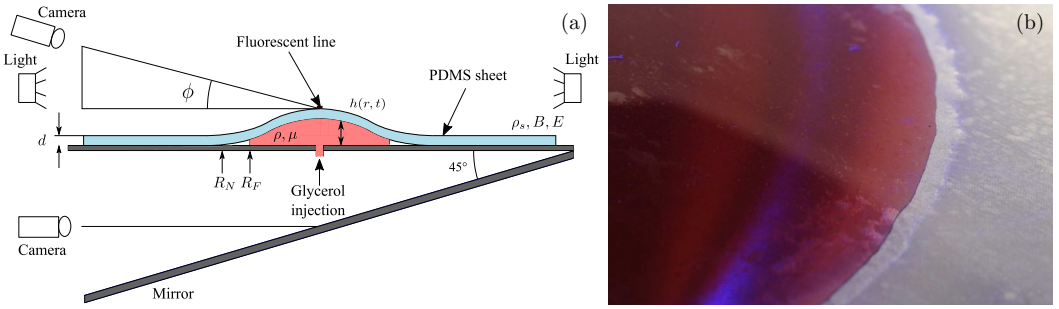

FIG. 1. (a) Schematic diagram of the theoretical model and experimental setup with the physical parameters in the system. (b) Photograph of an experimental fluid front showing the lag between the fluid front and fracture front.

no-slip conditions at the front [10] have been proposed to account for experimental observations. For the problem of a viscous fluid spreading underneath an elastic sheet, a macroscopic precursor film has been used to regularize this contact-line singularity [7], but this fails to explain fracturing phenomena, as found in magmatic intrusions, where there is no evidence of a prewetted surface.

We show through consideration of a simple lubrication model that a fluid lag, or vapor tip, between the fluid front and the fracture front can be used to regularize the tip (Fig. 1). The large negative pressure gradient at the tip is limited by the vapor pressure of the fluid, and hence the fracture front travels faster (at the elastic wave speed in the solid) while the fluid lags behind. This physical process leads to emergence of a fluid lag that regularizes the dynamics at the tip [12]. Importantly we demonstrate an experimental system capable of characterizing this vapor tip, thereby confirming its presence and role in the transient dynamics. A fluid lag has previously been invoked in other contexts, when modeling penny-shaped cracks [13] and buoyancy-driven fractures [14], and has been observed in laboratory experiments on the fracturing of elastic blocks [15–17] but has not been systematically characterised. Our development of a theoretical model and consistent laboratory experiments using thin elastica lead to a simpler analysis and treatment of fluid-driven fracturing and provides a usefully reduced system in which to understand the dynamics of fluid-driven fracturing, with direct biological and manufacturing implications.

To delaminate adhered elastica, the energy required to create new surfaces is $\Delta\gamma = \gamma_{SV}^{(\text{sheet})} + \gamma_{SV}^{(\text{substrate})} - \gamma_{SS}$, where γ_{SV} is the solid-vapor surface energy and γ_{SS} the solid-solid surface energy. This imposes a curvature at the fracture front, or fracture criterion, given by

$$\kappa = \sqrt{2}/l_{ec}, \quad \text{where} \quad l_{ec} = (B/\Delta\gamma)^{1/2} \tag{1}$$

is the elastocapillary length scale, with bending stiffness B. This curvature condition is obtained from an energy balance at the crack tip where the elastic strain energy in the sheet is balanced by the creation of new surfaces [18,19]. The quasistatic condition may be derived by energy minimization at the crack tip, and assumes a separation of scales between the fast fracturing dynamics and the relatively slow fluid dynamics driving tip propagation. The material strength of adhesion at the crack tip allows for the possibility of static solutions and controls the long-time behavior of spreading.

We show that two dynamical regimes are possible: viscosity dominant spreading controlled by the pressure gradient driving fluid into the vapor tip and adhesion dominant spreading controlled by interfacial adhesion. These two regimes are analogous to the limiting regimes of propagation for a semi-infinite hydraulic crack in an elastic medium [13]. In the elastic bending case considered here, we demonstrate an asymptotic model for propagation in the adhesion and viscosity dominated limits by resolving the behavior of the vapor tip.

We note that since submitting our manuscript for publication, we have been made aware of a recent publication that presents a comparable analysis of the problem of fluid-driven fracturing of

adhered thin elastica in which two regimes of propagation are described in the context of near-surface hydraulic fractures [20]. This work complements the mathematical approach taken here, where in addition the results of these analyses have been tested experimentally, demonstrating the formation of a vapor tip and different regimes of propagation.

This paper is structured as follows. Section II presents the static blister shapes and dynamic model demonstrating the transition from viscosity dominant to adhesion dominant spreading within the thin elastica framework. Section III describes the experimental setup and methods. Finally, the experimental results are analyzed and compared with the theoretical model in Sec. IV.

II. THEORETICAL MODEL

To examine the fluid-driven delamination of an adhered elastic sheet (see Fig. 1), a volume of fluid of density ρ and viscosity μ is injected beneath an elastic sheet of thickness d and density ρ_s initially adhered to a horizontal substrate with adhesion energy $\Delta\gamma$. Here, motivated by our experiments (discussed in Sec. III), we assume axisymmetric spreading and elastic deformation. In all dynamic cases the fracture front, R_N, extends beyond the fluid front, R_F, such that a vapor-filled tip exists of length $L = R_N - R_F$. The contribution to the pressure due to bending stresses dominates over contributions from tensional forces when the vertical deflection of the sheet is smaller than the thickness, $h(r,t) \ll d$. Hence the reduced pressure can be written as $\tilde{p} = p - p_0 - \rho_s g d = B\nabla^4 h + \rho g(h - z)$, where tension is neglected, p is the pressure in the fluid, and p_0 is a reference pressure with bending stiffness $B = Ed^3/12(1-\nu^2)$, where E and ν are the Young's modulus and Poisson's ratio of the sheet, respectively.

For large aspect ratios we may balance viscous drag with the hydrostatic and elastic pressure gradients to describe the deflection of the sheet [21],

$$\frac{\partial h}{\partial t} = \frac{1}{12\mu}\frac{1}{r}\frac{\partial}{\partial r}\left[rh^3\frac{\partial}{\partial r}(B\nabla^4 h + \rho g h)\right], \tag{2}$$

where global mass conservation gives

$$V(t) = 2\pi\int_0^{R_F} hr\,dr. \tag{3}$$

The balance between elastic stresses and gravity acting on the fluid gives rise to a natural horizontal, elastogravity length scale, $l_{eg} = (B/\rho g)^{1/4}$, and hence characteristic height and time scales may be defined as $H_0 = (12\mu Q/\rho g)^{1/4}$ and $T_0 = H_0 l_{eg}^2/Q$, respectively, where Q is a typical volume flux.

A. Static shapes

Adhesion of the sheet at the perimeter allows for the possibility of static solutions with no vapor tip, $R_N = R_F$, analogous to the capillary sessile drop [22]. The potential energy of the blister is balanced by the energy of adhesion between the elastic sheet and the horizontal substrate. For a constant volume V, this gives rise to static shapes with uniform pressure $\tilde{p}$. The potential energy of the blister has contributions from elastic deformation and from the gravitational potential. When the radius is smaller than the elastogravity length scale, $R_F \ll l_{eg}$, the pressure within the blister is dominated by bending stresses with $\tilde{p} \simeq B\nabla^4 h$. At the origin the imposition of zero slope and bending moment ensure that the mathematical description of the height of the sheet does not diverge as $r \to 0$. For static shapes the fracture and fluid fronts coincide, and continuity with the adjoining adhered regions requires that the height and gradient of the sheet are zero at the front, $h = \nabla h = 0$ at $r = R_F$. The deflection reduces to the classic bell-shaped form [23,24]

$$h(r) = \frac{\tilde{p}R_F^4}{64B}\left(1 - \frac{r^2}{R_F^2}\right)^2 \tag{4}$$

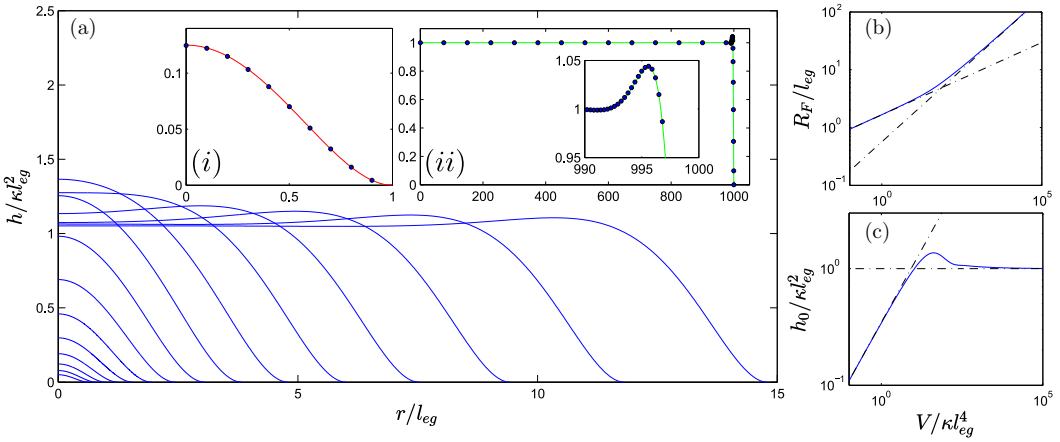

FIG. 2. (a) Plot of the static profiles for a constant volume V transitioning from bending to gravitationally dominated regimes. Inset (i) shows numerical solution in the pure bending regime (blue dots) plotted on top of theoretical profile (4) (red curve), and (ii) the numerical solution in the gravity dominant regime with a bending tip (blue dots) plotted on top of theoretical profile (6) (green curve). (b) Dimensionless radial extent with volume. (c) Dimensionless central deflection with volume.

[see Fig. 2(a)(i) (inset)]. Global mass conservation (3) and the curvature condition at the front due to adhesion impose $V = \pi \tilde{p} R_F^6/192B$ and $\kappa = \tilde{p} R_F^2/8B$, respectively, where $\kappa = \sqrt{2}/l_{ec}$ [6], and thus determine the radial extent and central deflection:

$$R_F = \left(\frac{24V}{\pi\kappa}\right)^{1/4} \quad \text{and} \quad h_0 = \left(\frac{3\kappa V}{8\pi}\right)^{1/2}. \tag{5}$$

In contrast, for larger volumes when the radius is much greater than the elastogravity length scale, $R_F \gg l_{eg}$, gravity becomes important, and the uniform pressure contains both elastic and hydrostatic contributions, $\tilde{p} = B\nabla^4 h + \rho g h$. In the interior, the pressure is nearly hydrostatic, and hence the height is uniform, $h \simeq h_0$, and the profiles are flat topped. Near the front, on a length scale $O(l_{eg})$, the hydrostatic pressure is balanced by elastic stresses due to bending the elastic sheet over the periphery. Adhesion at the fracture front imposes the curvature of the sheet as it touches down, $\kappa \sim h_0/l_{eg}^2$, which thereby determines the height of the static elastic droplet. (Note that for an axisymmetric blister the second radius of curvature, $\sim 1/R_F$, does not play a role in fracturing as the tip may be considered roughly two-dimensional for $R_F \gg h, d$.) An analytic solution can be found by matching the interior profile of uniform height with the peripheral bending region, where $p \simeq Bh^{IV} + \rho g h$. This gives profile

$$h(r) = \kappa l_{eg}^2 [1 - e^X(\cos X - \sin X)], \tag{6}$$

where $X = (r - R_F)/\sqrt{2}l_{eg}$ [see Fig. 2(a)(ii) (inset)]. In this sessile, elastic limit the radial extent and central deflection are

$$R_F = \left(\frac{V}{\pi\kappa l_{eg}^2}\right)^{1/2} \quad \text{and} \quad h_0 = \kappa l_{eg}^2. \tag{7}$$

Figure 2 shows the transition from bending dominant to gravitationally dominant profiles, radial extent, and central deflection with increasing volume (blue curves) along with asymptotic scaling from Eqs. (5) and (7) (black dot-dashed lines).

These static shapes arise due to the balance between adhesion of the elastic sheet and the substrate at the periphery and the hydrostatic and elastic potential energy of the blister. In Sec. II B we will

show that at late times, the dynamic spreading of the fluid blister transitions through a series of quasisteady equilibrium states given by these static solutions with $V = Qt$.

B. Dynamic spreading

In contrast to the static case, dynamic inflation leads to the emergence of a vapor tip. Viscous stresses diverge at the tip requiring a large pressure gradient to drive viscous fluid to the fracture front. The pressure in the fluid is limited by the vapor pressure, and hence the fracture front travels faster (at the elastic wave speed in the solid) while the fluid lags behind. This physical process regularises the dynamics at the tip by introducing a finite fluid thickness at the fluid front [12]. An examination of the dominant length scales at the tip reveal two possible behaviors when the volume $V(t) = Qt$; either the expansion of the fluid blister is controlled by viscous dissipation, or by the requirement to overcome the energy of adhesion.

At early times, $R_F \ll l_{eg}$, the evolution of the blister is slow so that the viscous pressure losses from the fluid input to the fluid front are small, and therefore the interior pressure is nearly constant. The deflection of the sheet in this limit takes the bell-shaped form described in (4). The rate at which the blister expands is determined entirely by processes at the fluid front. Assuming that the radial extent of the fluid greatly exceeds the length of the vapor tip, $R_F \gg L$, we can treat the tip region as two-dimensional with reduced pressure $\tilde{p}_T = p_T - p_0 - \rho_s g d = Bh^{IV}$, where $\sigma = -\tilde{p}_T$ is large and the vapor tip pressure p_T is negligible compared with atmospheric pressure p_0 and the weight of the beam [1,12]. For large values of σ the regularization is only felt over a small boundary layer near the fluid front. Hence the interior profile can be given by the static solution, (4). As in the static case, continuity at the tip requires the height and gradient to be zero $h = h' = 0$ with fracture criterion $h'' = \kappa$ at $r = R_N$. The deflection of the sheet in the vapor tip may then be written as

$$h(r,t) = -\frac{\sigma}{24B}(R_N - r)^3(R_N - r - L) + \frac{h(R_F,t)}{L^3}(R_N - r)^3 - \frac{\kappa}{2L}(R_N - r)^2(R_N - r - L), \tag{8}$$

for $R_F, R_N \gg h, d$, which extends the vapor tip model [[12], Eq. (3.5)] to include adhesion at the fracture front. From (8), it is apparent that the curvature at the fluid front is imposed by adhesion and the dynamics of the propagating fluid interface, $\kappa_F \simeq 2h(R_F,t)/L^2 \simeq \kappa + \sigma L^2/8B$. This defines a natural length scale $L_C = (B\kappa/\sigma)^{1/2}$ over which the curvature due to adhesion is felt. A comparison of this length scale with the size of the vapor tip, L, may be used to determine the dominant physics controlling spreading. When $L \gg L_C$ the curvature at the fluid front is dominated by the viscous fluid dynamics and spreading is in the viscosity dominant regime. In contrast, when $L \ll L_C$ the curvature at the front is imposed by the adhesion criterion, and spreading is adhesion dominant.

To determine the length of the lag region L and hence the spreading rate we look for a traveling wave solution near the fluid front of the form $h = h_F f[\xi \equiv (r - R_F(t))]$, which satisfies (2),

$$-\dot{R}_F h_F f' = \frac{Bh_F^4}{12\mu}(f^3 f^V)' \quad \Rightarrow \quad -\dot{R}_F = \frac{Bh_F^3}{12\mu} f^2 f^V, \tag{9}$$

using mass conservation at the fluid front $\dot{R}_F = \lim_{r\to R_F} -h^2 p_r/12\mu$, where $f' = \partial f/\partial\xi$, $f^V = \partial^5 f/\partial\xi^5$ and $p_r = \partial p/\partial r$. This balance at the fluid front may be used to define a viscous peeling length scale $l_p = (Bh_F^3/12\mu\dot{R}_F)^{1/5}$ [7]. We solve (9), along with three unknowns (R_F, h_F, and L), subject to matching the deflection and its first four derivatives at the fluid front (8), along with boundary conditions of constant interior curvature $f'' \to$ const, as well as f''', $f^V \to 0$ as $\xi \to -\infty$. In the viscosity-controlled regime, the curvature is $\kappa_F \simeq 2h_F/L^2 \simeq \sigma L^2/8B$, where l_p is the

dominant length scale at the tip and hence $L \simeq l_p$. The viscous peeling length scale is then

$$l_p = \left[\frac{2^{12}(12\mu)B^2\dot{R}_F}{\sigma^3}\right]^{1/7} \tag{10}$$

and demonstrates that spreading is viscosity controlled at early times providing $\dot{R}_F$ is sufficiently large, and hence $L \simeq l_p \gg L_C$. The fluid front exhibits a dynamic curvature that can be defined without recourse to adhesion [21],

$$\kappa_F \simeq \frac{2h_F}{L^2} \simeq \frac{\sigma L^2}{8B} \simeq \left[\frac{2^3(12\mu)^2\sigma}{B^3}\right]^{1/7} \dot{R}_F^{2/7}, \tag{11}$$

and it is this curvature which initially controls the propagation. Hence, this gives an evolution equation for the fluid front given an interior curvature κ_{int},

$$\dot{R}_F \simeq \left[\frac{B^3\kappa_{\text{int}}^7}{2^3(12\mu)^2\sigma}\right]^{1/2}. \tag{12}$$

Matching onto the interior curvature $\kappa_{\text{int}} = 24Qt/\pi R_F^4$ from (4) for a constant flux injection an asymptotic model for the radial extent, central deflection, and lag length in the viscosity dominant regime can be found,

$$R_F(t) = 1.52\left[\frac{Q^7B^3}{(12\mu)^2\sigma}\right]^{1/30} t^{3/10}, \tag{13}$$

$$h_0(t) = 0.41\left[\frac{(12\mu)^2\sigma Q^8}{B^3}\right]^{1/15} t^{2/5}, \tag{14}$$

$$L(t) = 1.19\left[\frac{(12\mu)^4B^9Q}{\sigma^{13}}\right]^{1/30} t^{-1/10} \tag{15}$$

(see the Supplemental Material [25]), where (13)–(15) are the axisymmetric generalizations of the two-dimensional results provided in Ref. [12]. We emphasize that these initial solutions are independent of the adhesion at the front.

At later times, $t > (12\mu)^{4/3}Q^{1/3}\sigma^{2/3}/B^2\kappa^5$, the decrease in the velocity $\dot{R}_F$, implies that $l_p \ll L_C$, and there is therefore a transition to adhesion control where the viscous peeling length scale no longer dominates the curvature at the tip. The curvature at the fluid front is predominantly that imposed by adhesion, $\kappa_F \simeq \kappa$, and the blister transitions through a series of quasistatic solutions, identical to those described by (5), now with $V = Qt$:

$$R_F(t) = \left(\frac{24Q}{\pi\kappa}\right)^{1/4} t^{1/4}, \tag{16}$$

$$h_0(t) = \left(\frac{3\kappa Q}{8\pi}\right)^{1/2} t^{1/2}. \tag{17}$$

Importantly, these late-time solutions are now independent of the fluid viscosity, as well as the presence (and hence length) of a vapor tip.

The lag length L may be calculated *a posteriori* by considering mass conservation at the fluid front, $\dot{R}_F \simeq h_F^2\sigma/12\mu L$, where there is a jump in pressure of $O(\sigma)$ at the fluid-vapor interface, and the curvature due to adhesion, $2h_F/L^2 \simeq \kappa$. Hence the lag length is determined by the slow flow of a viscous fluid infilling a wedge whose geometry is governed by adhesion:

$$L(t) = 0.82\left[\frac{(12\mu)^4Q}{\sigma^4\kappa^9}\right]^{1/12} t^{-1/4}. \tag{18}$$

It can be shown that the assumptions of constant interior pressure and pure bending ($r \ll l_{eg}$ and $h \ll d$) are valid provided $(12\mu B/Q\sigma^2)^{1/2} \ll t \ll l_{eg}^4\kappa/Q,\ d^2/Q\kappa$ by substituting the scalings for the two regimes into the original time evolution equation for the deflection (2). For axisymmetric spreading the transition from viscosity dominant to adhesion dominant spreading occurs at transitional horizontal, height, and timescales $R_C = (12\mu Q)^{1/3}\sigma^{1/6}/B^{1/2}\kappa^{3/2}$, $H_C = (12\mu Q)^{2/3}\sigma^{1/3}/B^{7/15}\kappa^2$, and $T_C = (12\mu)^{4/3}Q^{1/3}\sigma^{2/3}/B^2\kappa^5$, respectively. Note that these may occur before or after the transition to gravity.

In summary, dynamic spreading of a fluid beneath an elastic sheet is governed by a competition between elastic deformation of the sheet and either viscous dissipation or the energy required to overcome adhesion. At early times, the spreading is viscosity dominant, controlled by the pressure gradients driving viscous fluid into the tip, and given by the no-adhesion solution, [12]. When $l_p \ll L_C$, there is a transition to adhesion control, where the lag length no longer plays a role in the propagation of the fluid front and spreading is independent of viscosity of the fluid and pressure in the vapor tip. The regimes described here have parallels with those described for a semi-infinite hydraulic fracture evolving from a viscosity dominant to a toughness dominant crack in an elastic half-space [13] and, as shown in the following section, can be readily observed in experiments on thin elastica.

III. EXPERIMENTAL METHODS

Experiments conducted to investigate the fluid-driven fracturing of adhered elastica consisted of injecting a viscous fluid beneath an elastic sheet adhered to a horizontal substrate (see Fig. 1). An elastic sheet of polydimethylsiloxane (PDMS) was used with diameter 917 ± 1 mm and thickness $d = 9.8 \pm 0.3$ mm. The bending stiffness $B = 0.18 \pm 0.02$ Pa m^3 was measured using loop [26] and circular blister tests [27]. The PDMS sheet was manually adhered to a horizontal glass table using TUFFBond^{TM} Adhesive Mount Film of thickness 0.15 ± 0.01 mm. Glycerine-water solutions were injected between the glass table and composite PDMS and adhesive sheet. Injection was through a 5.5 mm diameter aperture, and the flux was determined by measuring the volume injected on the table from the deflection profiles.

The deformation of the PDMS sheet was measured by imaging a fluorescent line on top of the sheet at a known oblique angle ϕ, as shown in Fig. 1. To improve the contrast between the line and the background, the line was illuminated by a blue light and the blue color channel was isolated in the digital images acquired. A filtered image taken using this method is shown in Fig. 3(b) demonstrating the contrast achieved. Deflections of the line are determined by comparing with a reference image of the undeformed PDMS taken prior to injection. A Gaussian was then fit to the intensity profile across the line in a strip of pixels where the central peak was chosen as the centreline. To reduce scatter, an average was taken every 10 pixels. The final profile for this sample snapshot is plotted in Fig. 4 for time $t = 64$ s, viscosity $\mu = 2.12$ Pa s and volume flux $Q = 3.09 \times 10^{-7}$ m^3 s^{-1}.

The fluid and fracture fronts were measured by imaging from underneath the glass substrate using a mirror placed at 45° to the base [see Figs. 1 and 3(a)]. A high contrast between the fluid and the substrate meant the fluid front could be computed directly from the image using an edge-detection algorithm, as demonstrated in Fig. 3(c) by the black-dashed line. Due to the small, nonaxisymmetric deviations, a circle was fit to the points detected at the fluid front to give radial extent R_F at each time step.

Partial internal reflection within the vapor tip allowed for distinction between the fluid front and fracture front. This is demonstrated in Fig. 3(c) where the blue color channel is isolated and the contrast increased. The scatter in the brightness of the vapor tip meant the fracture front could not be determined from an edge-detection algorithm. As a result, the fracture front was manually tracked at 10 points around the edge of the blister. The red dots in Fig. 3(c) show the edge-detected R_F and manually picked R_N. The lag length is determined at each pair of points and an average is taken for each time step. The results of this procedure are shown in Fig. 3(d), with the error given by the standard deviation of the 10 points measured at each time step.

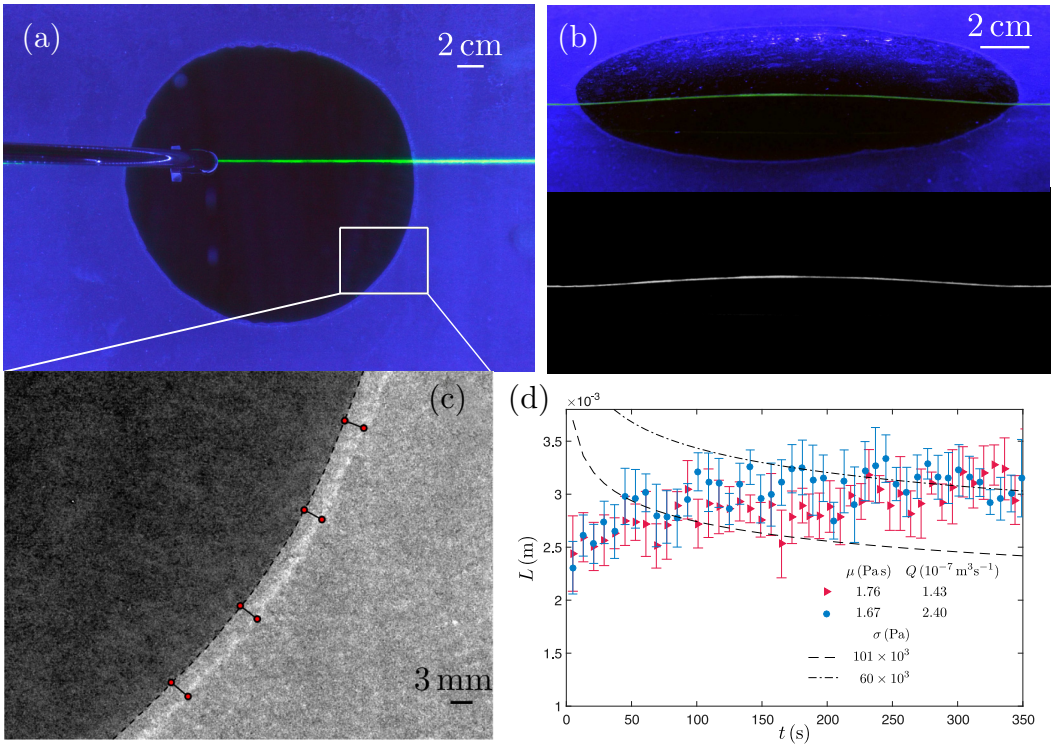

FIG. 3. Images of an experiment with viscosity and volume flux $\mu = 2.12\,\text{Pa s}$, $Q = 3.09 \times 10^{-7}\,\text{m}^3\,\text{s}^{-1}$, respectively, at $t = 64\,\text{s}$ taken from (a) underneath the experiment showing the radial extent and lag region (N.B.: the injection pipe is obscuring the left-hand side of the image), and (b) above at an oblique angle ϕ to the horizontal showing the fluorescent line painted on top of PDMS sheet with a filtered image showing the deflected line. (c) Expanded view of the edge of the experiment shown in (a) filtered to demonstrate intensity contrast between vapor tip and the substrate. Fluid front given by the black-dashed line with lag lengths given by pairs of red dots. (d) Lag length with time for two experiments in the viscosity dominant regime with different viscosities μ and volumes fluxes Q.

The adhesion energy $\Delta\gamma$ of the adhesive film was measured using a two-dimensional lift-off experiment. A 30 cm $\times$ 8 cm strip of PDMS was adhered to the glass table with the adhesive film. One end of the strip was uplifted using a micrometer in 0.2 mm increments and the resulting profile at each height determined by imaging a fluorescent line painted along the length of the strip. By translating the fracture position, the profiles can be collapsed onto one curve with the same tip structure. The curvature κ, and hence adhesion energy $\Delta\gamma$, can then be calculated by fitting a quadratic to the profiles (see Supplemental Material [25]). From four independent experiments, the curvature is measured to be $\kappa = 2.94 \pm 0.15\,\text{m}^{-1}$, and hence adhesion energy $\Delta\gamma = 0.78 \pm 0.17\,\text{Jm}^{-2}$. This adhesion energy is comparable to values previously obtained for similar tapes [18].

IV. RESULTS AND DISCUSSION

Using the PDMS sheet described above, the elastogravity length scale of $l_{eg} = 65\,\text{mm}$ restricts our experiments to a short radial range. Hence, in our current setup we cannot walk from one regime to another without the influence of gravity. As such we look at the viscosity and adhesion regimes separately. From our measurements of the adhesion energy and taking an estimate of the reduced tip pressure $\sigma = 101 \times 10^3\,\text{Pa}$ (which we will justify later when describing the measured lag length) we can calculate the transition timescale T_C. Table I lists the series of experiments carried out in

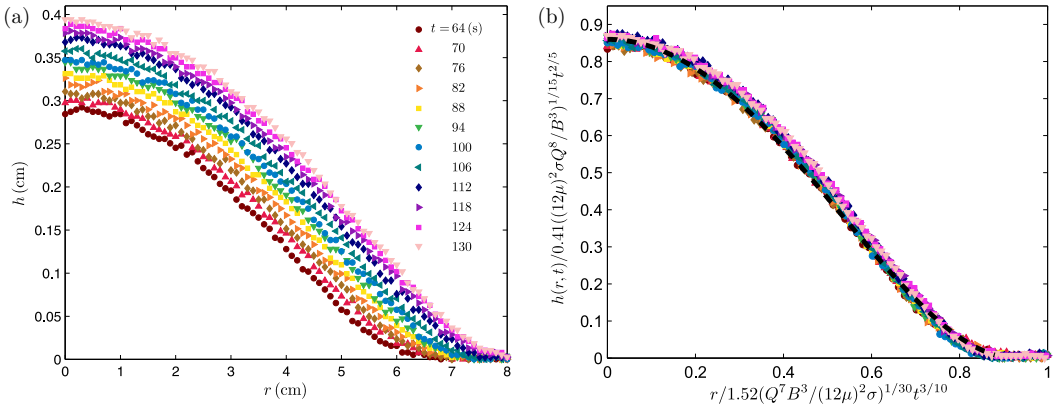

FIG. 4. Deflection profiles for an experiment in the viscosity dominant regime with viscosity $\mu = 2.12\,\text{Pa s}$, volume flux $Q = 3.09 \times 10^{-7}\,\text{m}^3\,\text{s}^{-1}$, $\sigma = 101 \times 10^3\,\text{Pa}$ for $t = 64$–$130\,\text{s}$, where $\Delta t = 6\,\text{s}$. (a) Measured deflection, and (b) deflection scaled with theoretical expressions (13) and (14). The black-dashed line shows the theoretical profile (4).

terms of viscosity μ and volume flux Q, where experiments 1–6 have a large transition timescale, $T_C = 93.0$–$154.1\,\text{s}$, and experiments 7–12 have a small transition timescale, $T_C = 0.4$–$5.7\,\text{s}$. By equating the expressions for the radial extent in the two regimes (13),(16), the time of transition $t_C = ((24/\pi)^{1/4}/1.52)^{20} \simeq 6.0 T_C$. Hence, we would anticipate experiments 1–6 to be in the viscosity dominant regime and experiments 7–12 to be in the adhesion dominant regime.

A. Viscosity dominant spreading

In experiments 1–6 in the viscosity dominant regime (see Table I), pure glycerine was used with viscosities $\mu = 1.67$–$2.12\,\text{Pa s}$ and volume fluxes $Q = (1.43 - 3.09) \times 10^{-7}\,\text{m}^3\,\text{s}^{-1}$. Figure 4 shows the measured deflection for an experiment with viscosity $\mu = 2.12\,\text{Pa s}$ and volume flux

TABLE I. Experimental parameters for 12 experiments with varying viscosities μ and volume fluxes Q. The transition timescale T_C is calculated using bending stiffness $B = 0.18\,\text{Pa m}^3$, reduced vapor tip pressure $\sigma = 101 \times 10^3\,\text{Pa}$, and measured curvature $\kappa = 2.94 \pm 0.15\,\text{m}^{-1}$. κ_{adh} is the tip curvature measured during experiments in the adhesion dominant regime and hence is not applicable to experiments 1–6 in the viscosity dominant regime.

Experiment	μ (Pa s)	Q (10^{-7} m^3 s^{-1})	T_C (s)	κ_{adh} (m^{-1})
1	1.76	1.43	93.0	n/a
2	1.76	1.74	99.3	n/a
3	1.69	2.12	100.5	n/a
4	1.67	2.40	103.1	n/a
5	1.78	2.83	118.4	n/a
6	2.12	3.09	154.1	n/a
7	0.17	1.64	4.3	2.91 ± 0.25
8	0.16	4.81	5.7	3.04 ± 0.28
9	0.15	1.58	3.6	2.53 ± 0.15
10	0.11	3.12	3.0	2.48 ± 0.26
11	0.07	1.56	1.3	2.03 ± 0.17
12	0.03	1.60	0.4	1.42 ± 0.26

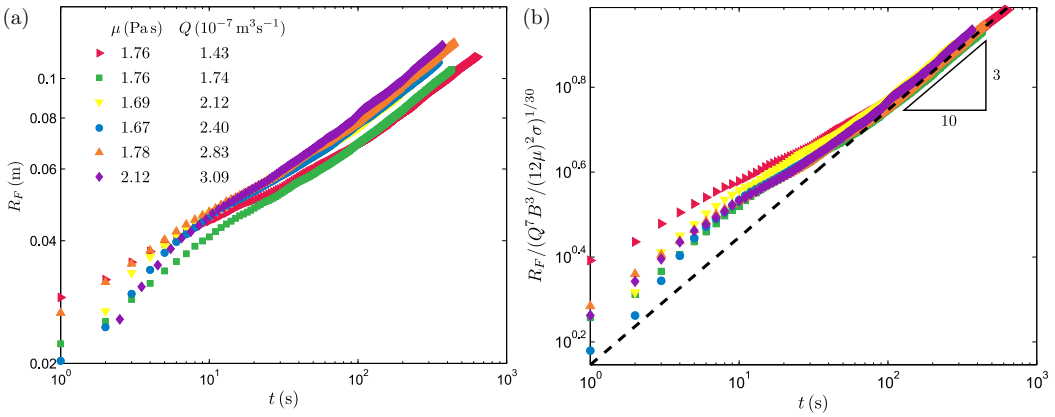

FIG. 5. Radial extent with time in the viscosity dominant regime. (a) Measured radial extent and (b) radial extent scaled with $\{Q^7B^3/[(12\mu)^2\sigma]\}^{1/30}$. Black-dashed line corresponds to best fit $R_F/\{Q^7B^3/[(12\mu)^2\sigma]\}^{1/30} = 1.40\,t^{3/10}$.

$Q = 3.09 \times 10^{-7}\,\mathrm{m^3\ s^{-1}}$ for $t = 64 - 130\,\mathrm{s}$, with profiles plotted every $\Delta t = 6\,\mathrm{s}$. From Sec. II, Eqs. (13) and (14) describe the radius and central deflection at time t in the viscosity dominant regime. By scaling the radius and height of the profiles in Fig. 4(a) by these expressions for R_F and h_0, the profiles collapse on to a universal curve described by (4); see Fig. 4(b). The black-dashed line shows the theoretical profile given by Eq. (4) demonstrating agreement with the collapsed data set. This confirms that in the dynamic spreading case the shape of the blister remains unchanged from the classic bell-shaped profile.

Because the pressure within the central blister was quasistatic, the position of the blister with respect to the injection hole was only weakly constrained and hence was very sensitive to initial experimental conditions. For example, the differing angle the injection pipe made to the horizontal substrate, or small differences in the adhesion energy in the immediate vicinity of the injection hole resulted in migration of the blister off-center [see Fig. 3(a)]. At the start of each experiment, the fluorescent line on the PDMS sheet was aligned with the injection hole, and hence for the same experiments the detected deflection profile is of a chord taken slightly off-center. For these reasons, the magnitude of the measured radius and height in Fig. 4(a) are less than the theoretical prediction for a profile through the origin, i.e., the dimensionless radial extent and central deflection in Fig. 4(b) are less than 1. However, providing the offset from the origin is sufficiently small, we would still anticipate a bell-shaped profile given by Eq. (4) as shown in the collapse of profiles in Fig. 4(b). Once the injected volume is large enough, the influence of this nonaxisymmetry subsides and hence does not influence the dynamics analyzed below.

Figure 5(a) shows the radial extent with time for six experiments with different volume fluxes in the viscosity dominant regime. In Fig. 5(b) the radial extent is scaled with $\{Q^7B^3/[(12\mu)^2\sigma]\}^{1/30}$ from Eq. (13). This scaling collapses the experimental data after the initial transient close to a common curve with power law exponent 3/10, in line with the theoretical scaling $R_F \sim t^{3/10}$ in the viscosity dominant regime. The black-dashed line in Fig. 5(b) corresponds to the best fit line $R_F/\{Q^7B^3/[(12\mu)^2\sigma]\}^{1/30} = 1.40\,t^{3/10}$, where the prefactor is within 8% of the theoretical prefactor 1.52.

For the viscosity dominant regime, we manually measured the lag length using the methods described in Sec. III [see Fig. 3(c)]. Figure 3(d) plots the lag length for two experiments with volume fluxes $Q = (1.43,\ 2.40) \times 10^{-7}\,\mathrm{m^3\ s^{-1}}$, where L is the average of the measured lag lengths and the error bars are one standard deviation above and below the mean. The overlapping error bars for the two experiments suggest there is no measurable difference between the lag lengths which is supported by the negligible dependence on the volume flux, $Q^{1/30}$, in Eq. (15). The black dashed and dot-dashed

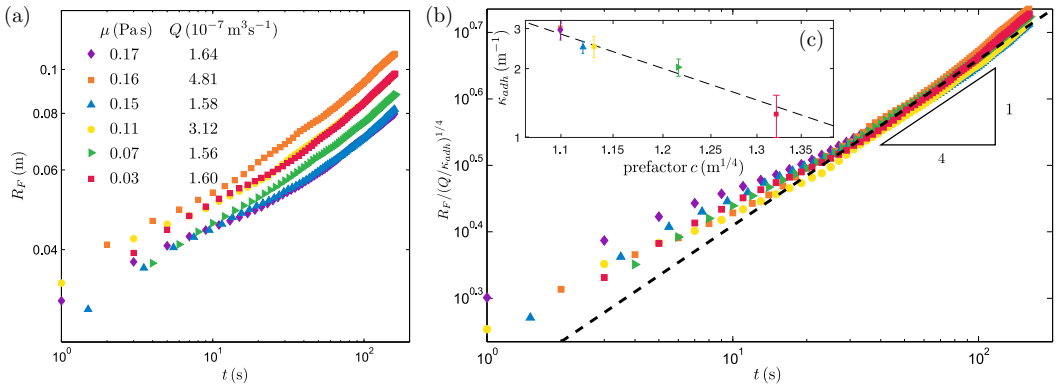

FIG. 6. Radial extent with time in the adhesion dominant regime. (a) Measured radial extent. (b) Radial extent scaled with $(Q/\kappa_{adh})^{1/4}$. Black-dashed line corresponds to best fit $R_F/(Q/\kappa_{adh})^{1/4} = 1.45\,t^{1/4}$. (c) (inset) Measured curvature κ plotted against measured prefactor c, where $R_F = c(Qt)^{1/4}$. Black-dashed line given by $c = 1.45\,\kappa_{adh}^{-1/4}$.

lines in Fig. 3(d) are Eq. (15) plotted with $\sigma = 101 \times 10^3$, 60×10^3 Pa, respectively. If the vapor tip produces a vacuum pressure at the front the vapor tip pressure would be zero, $p_T = 0$, and hence $\sigma = p_0 + \rho_s g d - p_T \simeq 101 \times 10^3$ Pa. The magnitude of the lag length observed suggests the tip pressure is non-negligible. Either some small amount of air may have been trapped when placing the adhesive sheet onto the glass substrate. These bubbles may act to increase the pressure at the tip and hence explain the smaller value of σ required to fit the lag length observed. Alternatively, some of the aqueous glycerine solution may have evaporated into the tip, suggesting that the pressure in the vapor tip is approximately equal to the vapor pressure.

The measured lag length also appears to be smaller at early times, in contrast to our theoretical prediction. However, it should be noted that Eq. (8) has been written in the limit $R_F \gg L$, which may be violated at early times. As a result, when fluid is first injected the elastic sheet is clamped at the radius of the injection hole, and the sheet is lifted up by the injection of fluid with a small lag length at the front. As the blister begins to propagate beyond this radius the lag length first increases as it relaxes to the dynamically determined extent. This transient behavior can be seen in Fig. 5(b) where the radial extent does not collapse at early times and in Fig. 3 where the lag length increases initially, and continues until the pressure decreases to that given by the elastic pressure, i.e., until the blister is large enough that the initial pressure buildup is negligible. The constant lag length observed at late time during the viscosity dominant spreading is then consistent with the slowly varying lag length $L \sim t^{-1/10}$ predicted by the theoretical model.

B. Adhesion dominant spreading

In experiments 7–12 (see Table I), in the adhesion dominant regime, glycerine-water solutions were used with viscosities $\mu = 0.03$–0.17 Pa s and volume fluxes $Q = (1.56$–$4.81) \times 10^{-7}$ m^3 s^{-1}. Figure 6(a) shows the measured radial extent with time. Under the assumption that the adhesion energy is constant and with fracture front curvature given by measured value $\kappa = 2.94 \pm 0.15$ m^{-1}, we scale the radial extent by $Q^{1/4}$ from Eq. (16) and find that the prefactor c, where $R_F = c(Qt)^{1/4}$, is dependent on the glycerol-water content of the injected fluid. From Eq. (16), c is a constant set by the curvature imposed by adhesion at the fracture front. Hence, we find that the curvature at the fracture front, which is constant for any given experiment, differs from the measured static value κ and varies with the fluid viscosity. The curvature, or equivalently the adhesion energy, is therefore a function of the glycerol-water content, with blistering a sensitive measure of the effective surface energy of the adhesive tape in response to interaction with a fluid. We independently measure the curvature κ_{adh} for

each experiment by fitting a quadratic to the tip region of the detected deflection profiles; see Table I. This demonstrates a decrease in curvature from the static measurement κ with decreasing viscosity. Figure 6(c) (inset) plots the measured curvature κ_{adh} against the prefactor c for the six experiments (see the Supplemental Material [25]). We find that $c = c(\kappa_{adh})$ where $c = 1.45\,\kappa_{adh}^{-1/4}$, black-dashed line, where the exponent of κ_{adh} agrees with the static scaling given by Eq. (16). In Fig. 6(b) the radial extent is scaled by $(Q/\kappa_{adh})^{1/4}$ using the measured values of κ_{adh}. This shows a collapse of the experimental data after the initial transient onto a common curve with power law exponent $1/4$, in line with theoretical prediction, where the black-dashed line is best fit $R_F/(Q/\kappa_{adh})^{1/4} = 1.45\,t^{1/4}$. The prefactor is within 13% of theoretical prefactor 1.66; this discrepancy is largely due to the inherent limitations in the measurement of experimental curvature κ_{adh}.

Unlike in the viscosity dominant regime, in the adhesion dominant regime no measurable lag region was observed during experiments; however, condensation droplets were seen when pulling off the adhesive tape. This suggests that the vapor tip was present and at low enough pressures to exsolve gas from the glycerine-water mix but was of sufficiently small scale such that it could not be distinguished from the fluid front during experiments using our optical technique. Substituting the experimental parameters μ, Q, and κ_{adh}, and taking $\sigma = 101 \times 10^3$ Pa, into the expression for the lag length in the adhesion dominant regime Eq. (18) gives $L \simeq 0.8$–1.2×10^{-3} m. This is consistent with a lag length which was below the image resolution as demonstrated in Fig. 3. We hypothesize that the decrease in curvature (and hence decrease in adhesion energy $\Delta\gamma$) with viscosity can be explained by a chemical interaction between the fluid and adhesive material when the lag length becomes small. This weakens the adhesive strength and hence reduces the curvature.

V. CONCLUDING REMARKS

Our theoretical model describes fluid-driven fracturing of adhered elastica by the introduction of a vapor tip separating the fracture and fluid fronts. Coupled with a fracture criterion imposed at the tip, this leads to the possibility of static shapes where the potential energy of the blister balances the energy required for fracture. For dynamic inflation, spreading can be split into two distinct regimes: viscosity dominant spreading controlled by the pressure gradient driving fluid into the vapor tip, and adhesion dominant spreading controlled by interfacial adhesion. Experiments using thin elastica adhered to a horizontal substrate have yielded consistent comparisons with theoretical predictions in the two regimes. The experimental techniques developed have also provided further evidence for the formation of an experimental vapor tip, again consistent with that proposed by the theoretical model. However, the nature of the tip region in terms of its small size have made measurement of the time evolution of the vapor tip difficult. In addition, the complexity of the adhesive due to the interaction with the glycerine-water solutions have made it challenging to characterize. This highlights that more work needs to be done to concretely nail down the role the tip plays in the dynamics. In particular, considering how alternative combinations of the injected fluid and adhesive tape could (a) make the tip easier to measure and (b) reduce the interaction between the fluid and the adhesive. Nonetheless, these experiments provide a simple setup to investigate fluid-driven fracturing of elastic media and observe the formation of a fluid lag, previously observed only in laboratory experiments on the fracturing of elastic blocks [15–17].

Static blister tests have long been used as a measure of the strength of adhesion between two materials [6,28]. The coupling of viscous fluid delaminating adhered elastica has moved concentration towards the study of blister dynamics [7,12] with application in a wide range of biological and industrial settings. These include the flow of biofluids through deformable vessels [8] such as the reopening of the pulmonary airways [29] and the manufacturing of stretchable electronics [5] made from buckled film on an elastomeric substrate [30]. The experiments described in Sec. IV have highlighted that blister dynamics could again usefully be applied to understanding the strength of adhesion with blistering providing a sensitive measure of the effective surface energy of the adhesive tape in response to interaction with a fluid. In addition, the treatment of using thin elastica coupled with an adhesive sheet has provided a simple, new approach to understanding fluid-driven fracturing

in an experimental setting. Hence, this experimental setup could lend itself to investigating other outstanding problems such as the effect of inhomogeneity in adhesive strength on the dynamics of fluid-driven fractures.

In Sec. II we described the static shapes for a given volume V and the dynamic spreading regimes for a constant flux injection, $V = Qt$. One can think of connecting these two cases by considering the evolution of a blister once injection has stopped at time $t = T$, or equivalently the dynamic spreading of a constant volume $V = QT$. As the in the constant flux case, spreading can be separated into two regimes: viscosity dominant spreading and adhesion dominant spreading. An evolution equation for the fluid front in the viscosity dominant regime can be found by substituting the interior curvature $\kappa_{\text{int}} = 24QT/\pi R_F^4$ from (4) into (12). Hence the fluid front is given by

$$R_F(t) = 1.68\left[\frac{(QT)^7 B^3}{(12\mu)^2\sigma}\right]^{1/30} t^{1/15}, \tag{19}$$

where the lag length decreases more rapidly than in the constant flux case with

$$L(t) = 0.97\left[\frac{(12\mu)^4 QTB^9}{\sigma^{13}}\right]^{1/30} t^{-2/15}. \tag{20}$$

In the adhesion dominant regime, the blister reaches the static shape (4) with constant radial extent and central deflection (5), where $V = QT$, with no lag between the fluid and fracture fronts. Equating these two expressions gives transitional timescale $T_{C_V} = 12\mu(QT)^{1/4}\sigma^{1/2}/B^{3/2}\kappa^{15/4}$. Hence, for a constant flux injection, if the injection is stopped at some time $t = T < T_{C_V}$ the blister will continue to propagate slowly in the viscosity dominant regime with radial extent (19) and decreasing lag length (20). When $t > T_{C_V}$, there will be a transition to adhesion control where the fracture front becomes stationary. Conversely, if $T > T_{C_V}$ the fracture front will become stationary when the injection is stopped. This provides a mechanism for stopping a fluid-driven fracture, something that is often overlooked when considering the propagation, say, of magmatic intrusions rather than requiring solidification.

ACKNOWLEDGMENTS

T.V.B. is funded by a NERC Ph.D. Studentship. J.A.N. is supported by a Royal Society University Research Fellowship.

[1] E. Detournay, Mechanics of hydraulic fractures, Annu. Rev. Fluid Mech **48**, 311 (2016).
[2] C. Michaut, Dynamics of magmatic intrusions in the upper crust: Theory and applications to laccoliths on Earth and the Moon, J. Geophys. Res. **116**, B05205 (2011).
[3] A. M. Rubin, Propagation of magma-filled cracks, Annu. Rev. Earth Planet. Sci **23**, 287 (1995).
[4] V. C. Tsai and J. R. Rice, A model for turbulent hydraulic fracture and application to crack propagation at glacier beds, J. Geophys. Res. Earth Surf. **115**, F03007 (2010).
[5] Y. Sun, W. M. Choi, H. Jiang, Y. Y. Huang, and J. A. Rogers, Controlled buckling of semiconductor nanoribbons for stretchable electronics, Nat. Nanotechnol. **1**, 201 (2006).
[6] T. J. W. Wagner and D. Vella, Floating Carpets and the Delamination of Elastic Sheets, Phys. Rev. Lett. **107**, 044301 (2011).
[7] J. R. Lister, G. G. Peng, and J. A. Neufeld, Viscous Control of Peeling an Elastic Sheet by Bending and Pulling, Phys. Rev. Lett. **111**, 154501 (2013).
[8] J. B. Grotberg and O. E. Jensen, Biofluid mechanics in flexible tubes, Annu. Rev. Fluid Mech. **36**, 121 (2004).

[9] D. Pihler-Puzović, P. Illien, M. Heil, and A. Juel, Suppression of Complex Fingerlike Patterns at the Interface between Air and a Viscous Fluid by Elastic Membranes, Phys. Rev. Lett. **108**, 074502 (2012).
[10] C. Huh and L. E. Scriven, Hydrodynamic model of steady movement of a solid/liquid/fluid contact line, J. Colloid. Interf. Sci. **35**, 85 (1971).
[11] M. H. Eres, L. W. Schwartz, and R. V. Roy, Fingering phenomena for driven coating films, Phys. Fluids **12**, 1278 (2000).
[12] I. J. Hewitt, N. J. Balmforth, and J. R. De Bruyn, Elastic-plated gravity currents, Eur. J. Appl. Math. **26**, 1 (2015).
[13] D. I. Garagash and E. Detournay, The tip region of a fluid-driven fracture in an elastic medium, J. Appl. Mech. **67**, 183 (1999).
[14] J. R. Lister, Buoyancy-driven fluid fracture: The effects of material toughness and of low-viscosity precursors, J. Fluid Mech. **210**, 263 (1990).
[15] W. L. Medlin and L. Masse, Laboratory experiments in fracture propagation, Soc. Petr. Eng. J. **24**, 256 (1984).
[16] A. P. Bunger, E. Detournay, and R. G. Jeffrey, Crack tip behavior in near-surface fluid-driven fracture experiments, C. R. Mécanique **333**, 299 (2005).
[17] A. P. Bunger, E. Gordeliy, and E. Detournay, Comparison between laboratory experiments and coupled simulations of saucer-shaped hydraulic fractures in homogeneous brittle-elastic solids, J. Mech. Phys. Solids **61**, 1636 (2013).
[18] T. J. W. Wagner and D. Vella, The 'Sticky Elastica': Delamination blisters beyond small deformations, Soft Matter **9**, 1025 (2013).
[19] N. J. Glassmaker and C. Y. Hui, Elastica solution for a nanotube formed by self-adhesion of a folded thin film, J. Appl. Phys. **96**, 3429 (2004).
[20] Z.-Q. Wang and E. Detournay, The tip region of a near-surface hydraulic fracture, J. Appl. Mech., Trans. ASME **85**, 041010 (2018).
[21] J. C. Flitton and J. R. King, Moving-boundary and fixed-domain problems for a sixth-order thin-film equation, Eur. J. Appl. Math. **15**, 713 (2004).
[22] L. H. Tanner, The spreading of silicone oil drops on horizontal surfaces, J. Phys. D Appl. Phys. **12**, 1473 (1979).
[23] S. Timoshenko and S. Woinowsky-Krieger, *Theory of Plates and Shells* (McGraw-Hill, New York, 1959).
[24] D. Pollard and A. Johnson, Mechanics of growth of some laccolithic intrusions in the Henry Moutains, Utah, II. Bending and failure of the overburden layers and sill formation, Tectonophysics **18**, 311 (1973).
[25] See Supplemental Material at http://link.aps.org/supplemental/10.1103/PhysRevFluids.3.074101 for discussion of the traveling wave solution and numerical analysis of Eq. (9), for measurement of the adhesion energy $\Delta\gamma$ of the adhesive mount film and for measurements of the front curvature κ_{adh} in experiments in the adhesion dominant regime.
[26] I. M. Stuart, A loop test for bending length and rigidity, Brit. J. Appl. Phys. **17**, 1215 (1966).
[27] B. M. Malyshev and R. L. Salganik, The strength of adhesive joints using the theory of cracks, Int. J. Fract. Mech. **1**, 114 (1965).
[28] H. M. Jensen, The blister test for interface toughness measurement, Eng. Fract. Mech. **40**, 475 (1991).
[29] M. Heil and A. L. Hazel, Fluid-structure interaction in internal physiological flows, Annu. Rev. Fluid Mech. **43**, 141 (2011).
[30] D. Y. Khang, J. A. Rogers, and H. H. Lee, Mechanical buckling: Mechanics, metrology, and stretchable electronics, Adv. Funct. Mater. **19**, 1526 (2009).